Targeting functionalised carbon nanotubes at the interphase of Textile Reinforced Mortar (TRM) composites

Cesare Signorini[a,*], Andrea Nobili[a,b]

[a]*Centro Interdipartimentale En&Tech, P.le Europa 1, 42124 Reggio Emilia, Italy*
[b]*Dipartimento di Ingegneria Enzo Ferrari, via Vivarelli 10, 41125 Modena, Italy*

Abstract

Performance of textile reinforced inorganic matrix composites depends on the matrix-to-fabric bond strength, the weak chain in the system. In this work, we investigate the role of multi-walled carbon nanotubes (MWCNT) dispersion in an amorphous silica nano-coating for AR-glass and carbon fabric Textile Reinforced Mortar (TRM) composites. Two lime mortars are considered at 56-day curing. Comparative mechanical testing in uni-axial tension show remarkable enhancements in terms of mean ductility, strength and energy dissipation capabilities. Besides, coating successfully prevents telescopic failure and delamination, which significantly narrows data scattering and benefits design limits. Crack pattern analysis reveals that coating promotes diffuse cracking in the specimen, with gradual and progressive damage buildup. Indeed, mean crack width and mean crack spacing are consistently reduced. BET, optical and E-SEM microscopy supports the action mechanism of the coating, that promotes wettability, surface roughening and imparts a remarkable increase in the specific surface area of the reinforcement.

Keywords: Textile Reinforced Mortar, Silica nano-coating, Carbon nanotubes, mechanical performance

*Corresponding author
Email address:* `cesare.signorini@unimore.it` (Cesare Signorini)

1. Introduction

Despite the interesting advantages that Textile Reinforced Mortar (TRM) composites display over the well-established class of Fibre Reinforced Polymer (FRP) composite materials [1], their application as externally-bonded reinforcement (EBR) for strengthening and retrofitting of existing structures is rather limited, in light of the poor bonding quality at the fibre-to-matrix interphase [2, 3, 4, 5]. Lack of compatibility between the fibres and the inorganic binder, as well as the presence of coarse aggregates in the mortar, result in unsatisfactory adhesion mechanisms, which trigger inconsistent failure modes, such as fabric delamination and telescopic failure. The latter is the typical failure mechanism in TRM, and consists of inner filaments in the fibres (the core) slipping over outer filaments (the sleeve) that are bonded to the mortar, as in the unfolding of a telescope. Indeed, the spacing between two adjacent fibres within a multifilament yarn (few microns) is several orders of magnitude lower than the average diameter of mortar grains, which is typically around $0.5 - 1$ mm. Consequently, mortar is unable to penetrate inside the filaments and bonds rest confined to the sleeve. In addition, poor chemical affinity (i.e. low hydrophilicity of the fibres) prevents from the formation of strong chemical bonds at the interphase, even for sleeve filaments. In contrast to FRP, the poor bonding quality affecting TRM/TRC impairs fibre-matrix congruence during deformation and, as a result, the rule of mixtures cannot be safely adopted to build reliable models [6]. Furthermore, failure occurs unreliably, according to multiple mechanisms, whence elevated scattering ensues. As a result, design limits are strongly penalized and the strengthening potential of the reinforcing fabric remains almost unexploited [7, 8].

A few attempts are documented in the literature to remedy this intrinsic weakness of TRM, most often directed at matrix modification [9, 10], also by CNT addition [11, 12]. In particular, polymeric modification of the inorganic matrix, that is admitted up to 5%wt over the inorganic component by the guidelines [13], goes under the name of Fibre Reinforced Cementitious Matrix

(FRCM) [3]. However, fibre coating appears as the most promising approach to bridge the performance gap between organic and inorganic composites, for it addresses precisely the matrix-to-fibre interphase. Specifically, capitalizing over the large body of expertise already developed for FRP, organic coatings represent the most natural option [14]. Evidence shows that organic coatings are capable of penetrating in between the reinforcing filaments and effectively prevent telescopic failure. In Donnini et al. [10], quartz sand is added to epoxy to roughen the matrix-to-fibre surface. Dvorkin et al. [15] experimentally document the reduction of fluid transport of aggressive ions inside carbon filaments induced by epoxy coating, thus promoting durability. In general, epoxy coatings have proved remarkably successful in enhancing mechanical performance, also through healing defects on the fibre surface [16]. Besides, fine-tuning epoxy formulation [17] and viscosity [18] highly improves the overall behaviour of coated TRM. It is noteworthy that the embedding matrix is capable of shielding the epoxy coating from the negative effects associated to high temperature exposure [19].

Nonetheless, the presence of an organic component is generally undesirable, mostly on the same grounds by which organic matrices are being replaced by inorganic binders. As a result, much interest lies in investigating inorganic coatings. As an example, silicon dioxide (in the form of micro-silica fume and silica nano-particles) exploits concentrated pozzolanic reactivity to good advantage, by strengthening the interphase zone (IZ), namely the thin mortar layer surrounding each fibre [20, 21]. Owing to its pronounced hydrophilic nature, silica appears as a promising fully-inorganic coupling agent, especially for alkali resistant glass (ARG) fabrics [22]. The addition of nano-fillers in the coating formulation can also be pursued and preliminary investigations are ongoing. In the paper by Cohen and Peled [23], mechanical performance of textile reinforced concrete (TRC) is assessed against the application of organic and inorganic nanofillers for inducing high friction resistance. Nano-particles suitable for this purpose comprise, among many, carbon-based fillers or organoclays [24, 25, 26]. In particular, multi-walled carbon nanotubes (MWCNT) are nested concen-

tric single-wall graphene hollowed particles with high aspect ratio (around 500) and specific surface area [27, 28]. Their outstanding tensile strength and stiffness, combined with negligible mass, make for a promising reinforcing technique [29, 30].

Kostopoulos et al. [31] highlight the role of MWCNT at improving impact and post-impact resistance of carbon FRP for aerospace applications. As discussed in the exhaustive review by Liew et al. [32], the adoption of CNTs in cementitious materials has been investigated only in fairly recent times, as an attempt at reducing micro-cracking within the conglomerate. In addition, CNT successfully dispersed in concrete have proved to improve the damping properties of cementitious composites [33]. This outcome is mainly due to the bridging effect exerted by CNT at the nanoscale and to the simultaneous reduction of the core porosity of the conglomerate [34, 35]. In a recent paper, Cui et al. [36] thoroughly examine how geometrical properties (e.g. tubes length and diameter) as well as functionalisation techniques of MWCNT tune the compressive and flexural response of concrete. According to these findings, the optimum aspect ratio of nanotubes should range at about 100 and hydroxyl-functionalised (namely highly hydrophilic) nanotubes convey remarkable strength gains, since the hydration products are diffusely and firmly bonded to the nano-fillers surface. Han et al. [37] point out that a CNT interpenetrated network in the conglomerate core favours leakage of hydration heat, thus reducing autogenous cracking. Finally, electrical conductivity of CNTs may impart smart sensing capabilities to structures, which become able to detect damage and incipient failure by carrying out time-scheduled non-destructive resistance measurements (see e.g. [38, 39] and references therein). Within the framework of cementitious materials, Irshidat and Al-Shannaq [40] study the dispersion of CNTs in in the cementitious embedding mortar of textile composites and provide strong evidence as to performance and durability enhancements. In the subsequent paper [12], they present the findings of an experimental program concerning bending of reinforced concrete (RC) beams strengthened with MWCNT-modified TRM laminates. As far as 1-ply laminates are concerned, the most impressive

4

results regards the initial stiffness of the reinforced beam, rather than the flexural capacity, which appears highly sensitive to the binder's formulation. All the aforementioned contributes agree on the fundamental role played by surfactants, which unlock the remarkable benefits of well dispersed unbundled CNTs [41, 42, 43].

In this paper, we consider a 0.5% wt. stabilized suspension of MWCNTs in an amorphous silica coating solution for application on synthetic continuous fibres, namely alkali resistant (AR) glass and carbon. In contrast to the existing literature, we consider a functionalised dispersing medium (i.e. silica sol) and modification is restricted to the fibres' surface, as opposed to modification of the embedding matrix. Compared to control specimens, remarkable improvements in terms of ultimate strength, ductility and energy dissipation capability are found. This outcome is related to a dramatic increase of the fabric specific area, accompanied by important enhancement in terms of hydrophilicity, i.e. the capacity to establish stronger chemical fibre-to-matrix cross-links. Optical and E-SEM microscopy reveal that CNT-induced surface roughness effectively prevents telescopic failure and fabric slippage inside the matrix.

2. Materials and methods

2.1. Materials

Two different fine-grained lime-based mortars and two reinforcing textiles are considered.

Physical, compositional and mechanical properties are gathered in Table 1. The first mortar, labelled MS (Lime Mortar, $f_{ck} = 5\,\text{MPa}$), consists of a natural hydraulic lime-based mortar with siliceous and carbonatic aggregates. Cement content is lower than 5%wt. The second mortar, tagged GC (Hybrid Mortar, $f_{ck} = 15\,\text{MPa}$), presents coarse aggregates (up to 1.4 mm diameter) and blended lime and cement binder [17].

Two different multifilament fabrics are considered as the reinforcing phase (Figure 1): AR glass (G) balanced biaxial mesh with open square grid and high-tenacity carbon (C) uniaxial fabric with ARG yarns in the weft direction. The

5

Characteristic	Unit	MS	GC
Aggregate maximum size	mm	1.0	1.4
Density (fresh state, UNI 1015-6)	kg/dm^3	1.50	1.73
Min. compression strength at 28 days	MPa	5.0	15.0
Min. flexural strength at 28 days (EN 196/1)	MPa	1.0	3.4
Adhesion strength at 28 days	MPa	0.4	1.0
Water content	%	21	21
Longitudinal elastic modulus (EN 13412)	GPa	n.a.	9.0

Table 1: Mortars' properties (as provided by the manufacturer)

main mechanical properties of the fabrics are displayed in Table 2. Fabrics are coated with a sol-gel silica solution where MWCNTs are dispersed. MWCNTs (Sigma, Merck Group) properties are reported in Table 3.

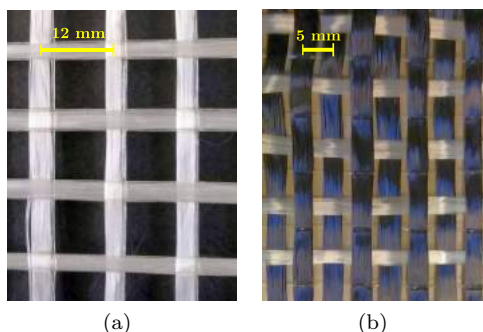

Figure 1: AR-glass (a) and carbon (b) multifilament fabrics are considered as the reinforcing phase

2.2. Amorphous silica nano-coating with dispersed MWCNT

CNT dispersion is obtained taking advantage of the water excess required to accommodate hydrolysis of the acid-catalysed silica sol-gel. A stable CNT aqueous dispersion is obtained by adding sodium dodecyl benzene sulfonate (NaDBS) as surfactant, as reported in the research by Haghgoo et al. [44]. In a covered beaker, a 3.3%wt solution (with respect to deionized water) of CNTs is mixed with NaDBS powder in a 2:3 CNT/NaDBS weight ratio. The suspension is placed on a magnetic stirrer for 5 minutes and then sonicated for 60 minutes, in order to allow the surfactant to distribute within the nanotubes interstices and favour disaggregation [45]. The suspension is added to TEOS/isopropyl

Characteristic	Unit	G	C
Yarn count	g/km	1200	800
Total (warp) specific weight per unit fabric area	g/m^2	300 (150)	220 (150)
Grid spacing (along the warp direction)	mm	12	5
Dry fabric cross-sectional area (per unit width), A_f	mm^2/cm	0.72	0.88
Ultimate strength along warp with epoxy (per unit width)	kN/cm	0.72	1.80
Elastic modulus, E_f	GPa	74	240

Table 2: Multifilament fabrics properties (as provided by the manufacturer)

Characteristic	Unit	Value
Density (at 25°C)	g/cm^3	2.1
Bulk density	g/cm^3	0.06 ÷ 0.08
Outside diameter	nm	10
Inside diameter	nm	4
Length	nm	4000
Aspect ratio	–	350 ÷ 550
Walls	No.	6 ÷ 8
Surface area (BET)	m^2/g	280 ÷ 350
Surface resistivity	Ω/sq	700 ÷ 900
Melting Point	°C	3652 ÷ 3697

Table 3: Multi-walled carbon nanotubes properties (as provided by the manufacturer)

alcohol solution together with nitric acid in stoichiometric ratio to trigger sol-gel transition, see also [46]. The silica solution, with an overall CNT weight ratio of 0.5%, is stirred for 2 hours at 50°C and then sonicated for further 15 minutes before fibres' dip-coating. Cut-to-size textiles are then immersed for 5 minutes in the suspension and subsequently left at laboratory conditions for a few minutes. Finally, fabrics are dried in a muffle at 110 °C for 15 minutes.

2.3. Experimental programme

2.3.1. Coating quality assessment

Fibre hydrophilicity is measured through a Brunauer-Emmett-Teller (BET) analysis [47], which is commonly used to gain insight on the specific (per unit mass) surface area (SSA) of a solid. SSA is an indicator of the adsorption and of the reactive capability of a surface. BET provides an accurate evaluation of

the SSA of a material at the solid phase by expressing its nitrogen adsorption as a function of relative pressure. SSA is evaluated by computing the amount of adsorbate gas corresponding to a monomolecular layer on the surface of the material. This technique encompasses both external surface and pore area to determine the total SSA. Fabric specimens weighting between 0.5 and 1 g are coated and then dried overnight at 60°C to remove residual humidity. Finally, measurement is performed in a Gemini V2.00 porosimeter (Micromeritics) on both uncoated and MWCNT coated fabric. Coating quality and uniformity are determined through optical stereo-microscopy (Leica EZ4D) and environmental scanning electron microscopy (E-SEM, Quanta-200, Fei Company).

2.3.2. Mechanical testing

Comparative uni-axial tensile tests are carried out on TRM specimens with (S-CNT) and without (control group, UC) silica coating with dispersed MWC-NTs. Specimens are manufactured on an individual basis by means of a dis-mountable polyethylene formwork and each test group consists of at least four specimens. 1-ply prismatic laminates are manufactured following the recent guidelines [48, 49], as detailed in [50, 51]:

- The first layer of fresh mortar is applied on the lubricated formwork in between two constraining removable laths, which provide guideline for the prescribed thickness of the embedding layer and for fabric placing.

- The reinforcing textile, either uncoated (UC) or S-CNT pre-preg, is placed on the fresh mortar onto which it is gently pressed to promote mortar interlocking.

- The mortar over-layer is then applied in between a second set of constrain-ing laths, that is stacked on top of the first.

- Specimens are cured for 7 days, tightly wrapped in a polypropylene self-detaching bag to simulate moist-curing.

- Finally, specimens are stripped and stored at laboratory conditions ($T =$

8

(20 ± 2)°C, $RH = (65\pm5)\%$) for 49 days. Indeed, 56-day curing is proven to positively affect durability for lime-based composite laminates [52].

- Prior to testing, two pairs of 100-mm long G-FRP tabs are epoxy glued at the specimen ends to accommodate the gripping mechanism at testing.

Specimens have prismatic shape (coupons), are 7-mm thick and their gauge length is $L_g = 250$ mm. Width equals 36 mm or 32 mm, and it is designed as to accommodate 3 or 7 strands, respectively for ARG and carbon fabric. Tensile tests are carried out on an electro-mechanic Instron 5567 universal testing machine (UTM), equipped with a 30 kN load cell. The clamping system consists of two hinges connected with stainless steel wedge clamps that apply lateral friction to the laminates. The test set-up is compliant with the prescriptions of the most common guidelines for characterization of Fibre Reinforced Cementitious Matrix (FRCM) composite materials [53]. Tests are carried out under displacement control at the nominal displacement rate of 0.50 mm/min. DIC analysis lends the actual elongation rate by subtracting the contribution of the sliding motion at the clamp-to-coupon interface. The latter is usually about 10% of the nominal rate [54].

Before embedment, uncoated and pre-preg (coated) fabrics are investigated through optical stereo-microscope LEICA EZ4D and environmental scanning electron microscope (E-SEM, Quanta FEI, The Netherlands) to evaluate the quality of the surface coating. During testing, the crack pattern evolution is recorded by DIC. Finally, failed specimens are investigated through optical microscopy, in order to characterise the distribution of carbon nanoparticles on the fibres surface and the quality of the impregnation.

3. Results and discussion

3.1. Coating characterization

3.1.1. Surface analysis and hydrophilicity

The effect of the coating on the SSA is well illustrated in the bar-charts presented in Fig.2, where a logarithmic scale is adopted. A remarkable increase
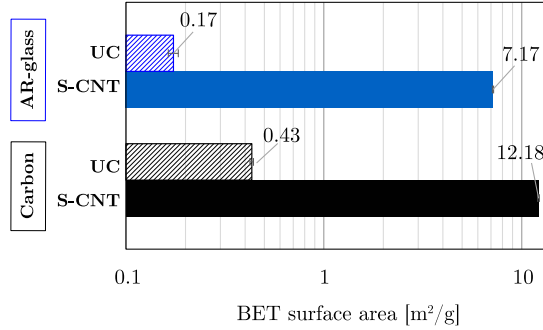
9

Figure 2: Specific surface area (SSA) for uncoated (UC) and silica+carbon nanotubes (S-CNT) coated fabrics, as obtained by BET analysis (logarithmic scale)

of the surface area is clearly achieved through S-CNT coating, and the relative outcome is even more pronounced for glass fibres. This outcome is not entirely unexpected given the affinity of glass with silica. Coating conveys a surface area enhancement that fares about 40 and 27 times the SSA of the control group, respectively for glass and carbon. This notable increase of surface area may effectively promote the hydrophilicity of the fabric and thus the adhesion capacity at the interphase. The accuracy of BET measurements is supported by the coefficient of determination in the linear regression of the BET diagram $(v^{-1}\varphi(1-\varphi)^{-1}$ vs $\varphi)$, that is practically 1 except for the G-UC sample ($R^2 = 0.794$), due to the extremely low SSA. In the BET diagram, v represents the mass of adsorbed gas and φ is the ratio between the equilibrium and the saturation pressure of adsorbates at the temperature of adsorption [47]. Typical BET diagrams are presented in Figure 3.
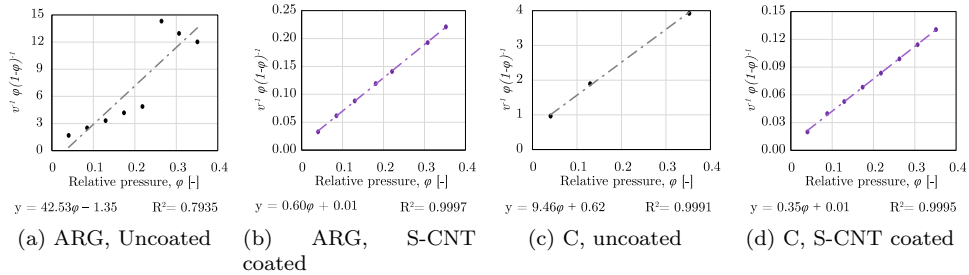

| (a) ARG, Uncoated | (b) ARG, S-CNT coated | (c) C, uncoated | (d) C, S-CNT coated |

Figure 3: BET diagrams for all the tested groups

217

3.1.2. Optical and E-SEM microscopy

Quality and uniformity of the coating are investigated through optical and electron microscopy. Figures 4(a) and (c) present an optical investigation of the surface of uncoated glass and uncoated carbon textiles, respectively, to be compared with the corresponding coated specimens, Fig.4(b) and (d). In the case of glass fibres, the presence of bundles of CNT, which stand out of the clear background, is quite evident. Conversely, CNT presence on carbon fibres can be appreciated only when light shines at a large incident angle to the sample surface. Sharper results are obtained through E-SEM: Figure 5 shows a single carbon coated multifilament yarn at $1000\times$ and $4000\times$ magnification. The presence of CNT individual nano-particles cannot be singled out, most likely as a result of the embedding role of silica molecules that surround CNTs. Yet, fibres appear coated by a thin layer of silica, which can penetrate inside the inner part of the yarn. Patches of residual salt deposits, most likely due to the surfactant employed to disperse CNTs, are seldom identified on the fibres through an energy dispersive X-ray (EDX) microanalysis.

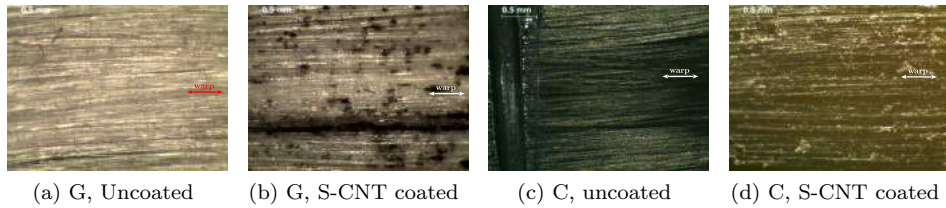(a) G, Uncoated   (b) G, S-CNT coated   (c) C, uncoated   (d) C, S-CNT coated

Figure 4: Optical stereo-microscopy investigation for AR-glass (a-b) and carbon (c-d) fabrics without and with S-CNT coating

3.2. Mechanical tests
3.2.1. Glass fabric

Figure 6 presents mean strength (i.e. stress-strain) curves for AR-glass textiles embedded in MS and GC mortar. An almost perfectly tri-stage behaviour is consistently observed across the S-CNT coated groups. The first stage is elastic and it holds until the first cracking strength (FCS) is attained. The elastic stage is followed by an intermediate regime (cracking stage) characterized by
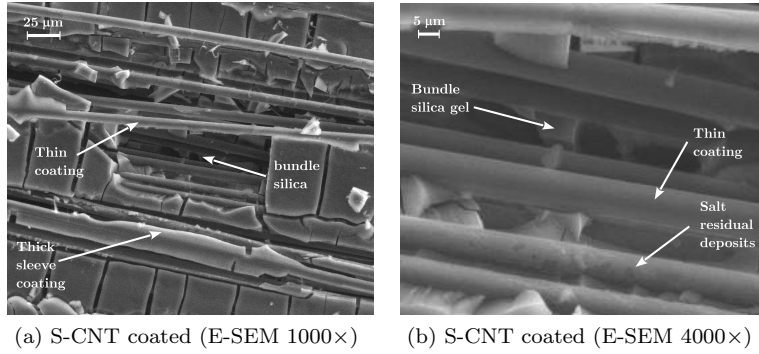
(a) S-CNT coated (E-SEM 1000×)   (b) S-CNT coated (E-SEM 4000×)

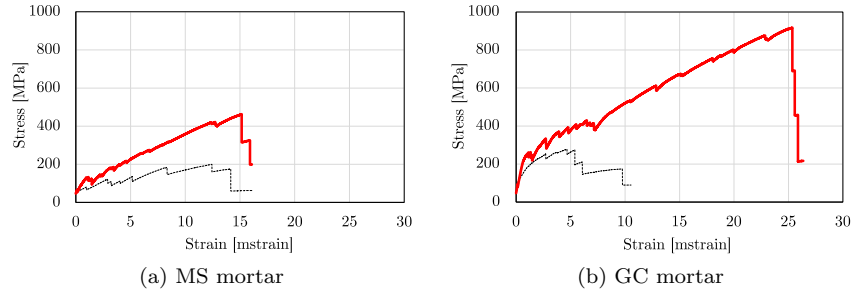Figure 5: E-SEM investigation for carbon fabrics with S-CNT coating

(a) MS mortar   (b) GC mortar

Figure 6: Mean stress-strain curves for uncoated (UC, black fine-dashed) and coated (S-CNT, red solid) glass fabric-reinforced coupons. $(1\,\mathrm{mstrain} = 10^{-3}\mathrm{mm/mm})$

the opening of several successive cracks. This regime ends when new cracks cease to appear and the existing ones widen. In this final, post-cracking stage, the specimen is more compliant (i.e. less stiff) than in the elastic regime, owing to the absence of the mortar contribution. The formation of several new cracks at the cracking stage is supported by many small stress drops in the strength curve, which account for the appearance of a diffuse cracking pattern. This, in turn, leads to high levels of mechanical energy being dissipated at failure (toughness) [55]. In stark contrast, the cracking stage appears very shortly in the uncoated specimens, where wide-spaced large cracks immediately develop with irreversible damage to the interphase, as a consequence of the high bursts of mechanical energy that are being released and cannot be dealt with elastically by the interphase. Accordingly, failure at the interphase brings about detachment between the fabric and the embedding mortar, sliding of the fibres and

²⁵⁴ internal delamination. On the overall, this mechanism possesses a lower bearing
²⁵⁵ capacity than that in the coated group. For these reasons, CNT-coating pro-
²⁵⁶ vides remarkable improvement both in terms of strength and ductility, that is
particularly striking for the hybrid lime-cement mortar (namely, mortar G).
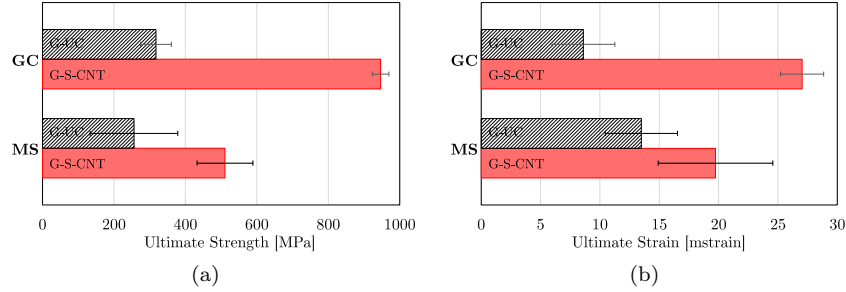

Figure 7: Ultimate strength (a) and strain (b) with $\pm$ 1 standard deviation band for uncoated (UC, grey) and coated (S-CNT, red) groups for all G-TRM.

²⁵⁷

²⁵⁸ A bar-chart comparison of the mean ultimate tensile strength (UTS) and
²⁵⁹ elongation of G-TRM composites at failure is presented in Figure 7. Labels
²⁶⁰ code for mortar (GC or MS), reinforcing fabric (G or C) and coating (S-CNT)
²⁶¹ or lack thereof (UC). For example, GC-G-UC stands for GC-matrix reinforced
²⁶² with uncoated glass fabric. It is very important to observe that coating sig-
²⁶³ nificantly decreases data scattering, especially for GC mortar, and this has a
²⁶⁴ strong positive bearing on design limits [21]. In fact, this very outcome is es-
²⁶⁵ pecially valuable for TRC/TRM materials, whose inconsistent performance is
²⁶⁶ their major drawback.

²⁶⁷ The beneficial effect of the coating on mechanical performance of G-TRM
²⁶⁸ specimens is best appreciated through the data provided in Table 4, which
²⁶⁹ compares the mean ultimate tensile strength, $\mu(f_u)$, mean elongation, $\mu(\varepsilon_u)$,
²⁷⁰ and mean dissipated energy, $\mu(W_u)$, across all tested groups, together with the
²⁷¹ relevant standard deviation. There, $\mu(\cdot)$, $\varsigma(\cdot)$ and CoV represent the mean
²⁷² value, the standard deviation and the coefficient of variation of the sampling,
²⁷³ respectively; $\Delta(\cdot)$ provides the percent variance of the relevant quantity in the
²⁷⁴ coated against the uncoated group. In order to take into account data scattering,
²⁷⁵ characteristic values (5%–fractile) are computed through Eqn.(1), assuming that

m	UC				S-CNT				Δ	
	$\mu(f_u)$	$\varsigma(f_u)$	CoV	$f_{u,k}$	$\mu(f_u)$	$\varsigma(f_u)$	CoV	$f_{u,k}$	$\Delta\mu(f_u)$	$\Delta f_{u,k}$
	[MPa]	[MPa]	[%]	[MPa]	[MPa]	[MPa]	[%]	[MPa]	[%]	[%]
MS	256	123	48	54	511	78	15	383	+100	+600
GC	317	43	14	246	947	23	2	909	+198	+270
	$\mu(\varepsilon_u)$	$\varsigma(\varepsilon_u)$	CoV	$\varepsilon_{u,k}$	$\mu(\varepsilon_u)$	$\varsigma(\varepsilon_u)$	CoV	$\varepsilon_{u,k}$	$\Delta\mu(\varepsilon_u)$	$\Delta\varepsilon_{u,k}$
	[mstrain]	[mstrain]	[%]	[mstrain]	[mstrain]	[mstrain]	[%]	[mstrain]	[%]	[%]
MS	13.5	3.0	23	8.6	19.7	4.8	24	11.8	+46	+38
GC	8.6	2.7	31	4.2	27.0	1.8	7	24.0	+214	+476
	$\mu(W_u)$	$\varsigma(W_u)$	CoV	$W_{u,k}$	$\mu(W_u)$	$\varsigma(W_u)$	CoV	$W_{u,k}$	$\Delta\mu(W_m)$	$\Delta W_{u,k}$
	[J/mm^3]	[J/mm^3]	[%]	[J/mm^3]	[J/mm^3]	[J/mm^3]	[%]	[J/mm^3]	[%]	[%]
MS	2.10	1.11	53	0.28	5.93	1.15	19	4.0	+183	+1346
GC	2.65	0.60	22	1.67	16.1	0.91	6	14.6	+508	+777

Table 4: Glass reinforcement – Mean UTS $\mu(f_u)$, mean strain $\mu(\varepsilon_u)$ and mean dissipated energy $\mu(W_u)$ across all tested groups, alongside their standard deviation ς, coefficient of variation CoV and percent variance Δ. $f_{u,k}$ is the characteristic strength in a normal distribution

data are normally distributed [56].

$$(\cdot)_k = \mu(\cdot) - 1.64\,\varsigma(\cdot) \tag{1}$$

The corresponding percent variance of the coated vs the uncoated group is denoted by $\Delta f_{u,k}$. We observe a striking five-fold increase in the mean dissipated energy for coated specimens embedded in the GC mortar against uncoated ones, as a combination of enhanced ultimate strength (+198%) and elongation (+214%). For the MS mortar, the corresponding result is also very significant, albeit not so impressive (+183%). Most significantly, data scattering is also strongly reduced by CNT-coating: consideration of the CoV for strength in the MS mortar (GC mortar) jumps from 48% (14%) in the UC group to 15% (2%) in the coated group. Similar observations can be made for elongation and energy dissipation. Such results support the idea that consistency in ultimate performance is strictly connected to the suppression of telescopic failure and of intralaminar textile sliding, which are inherently inconsistent mechanisms.

Stereo-microscopy provides clear evidence of interphase compatibility improvement, as in Figs.8 and 9 referring to the surface of glass fibres emerging in
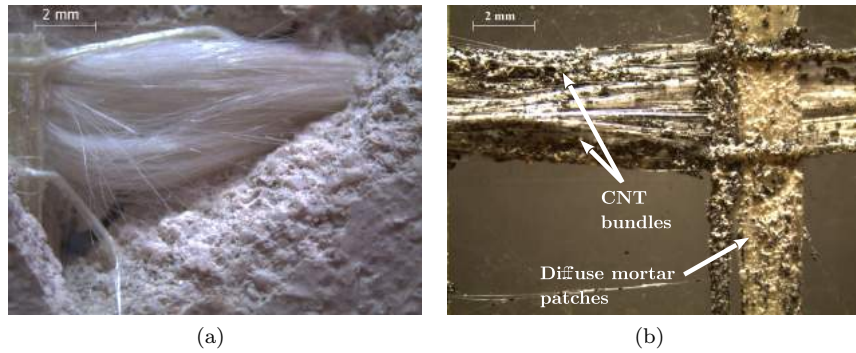
Figure 8: 8X magnification of uncoated (a) and coated (b) glass yarns at failure.
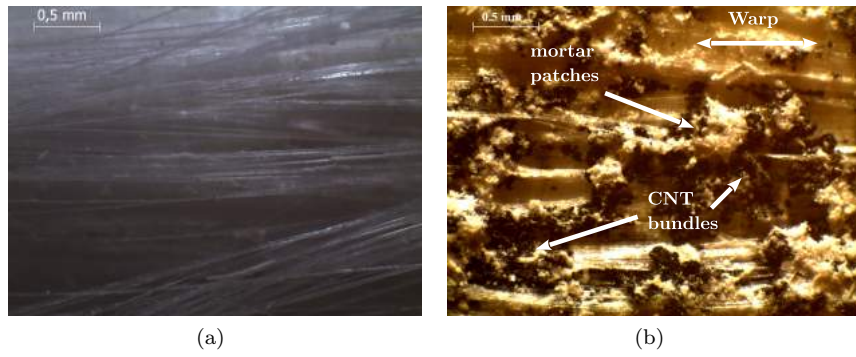

Figure 9: 35X magnification of uncoated (a) and coated (b) glass yarns at failure.

²⁹¹ the failure zone. Indeed, while UC strands are clean as they have been "pulled-
²⁹² out" as a result of telescopic sliding (unfolding generates misalignment of the
²⁹³ filaments of a single yarn), fibres in the S-CNT group maintain good alignment
²⁹⁴ and to them many mortar patches and CNT bundles are diffusely attached.
²⁹⁵ The distribution of MWCNTs appears not uniform over the fibre surface, which
²⁹⁶ fact enhances micro-roughness and prevents slippage with the mortar at the
²⁹⁷ interphase. In addition to providing a functionalising dispersing medium, silica
²⁹⁸ enhances the chemical interlocking with the mortar and bonds fibres together
²⁹⁹ [46]. To these benefits, the contribution of CNT is superposed and it consists of
³⁰⁰ strengthening the interphase zone and the fibre-to-matrix adhesion capability.

³⁰¹ *3.2.2. Carbon fibres*

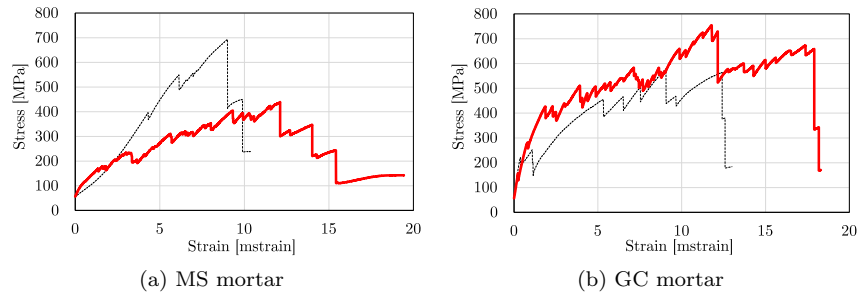(a) MS mortar   (b) GC mortar

Figure 10: Mean stress-strain curves for uncoated (UC, black fine-dashed) and coated (S-CNT, red solid) carbon-fabric reinforced specimens

³⁰²   Similar considerations may be put forward with regard to specimens rein-
³⁰³ forced with uniaxial carbon fabric. However, as already observed in Signorini
³⁰⁴ et al. [51], silica coating appears less effective on carbon fabric than on AR-
³⁰⁵ glass. This can be ascribed to the lower chemical affinity of the silica-carbon
³⁰⁶ system, as compared to silica-glass. In fact, the latter is expected to perform
³⁰⁷ significantly better, as a result of the chemical composition of the coating and
³⁰⁸ of the substrate being essentially the same. A consistent picture emerges when
³⁰⁹ MWCNTs act as high-strength interphase nanofillers in the coating. Figure
³¹⁰ 10 presents the mean stress-strain curve in uni-axial tension obtained for ms
³¹¹ and GC mortars. Strikingly, coating impairs performance in the MS mortar,
³¹² although this negative outcome is compensated by significant benefits in terms

of ductility and the overall effect is positive for mean energy dissipation (yet neutral in terms of characteristic value) .
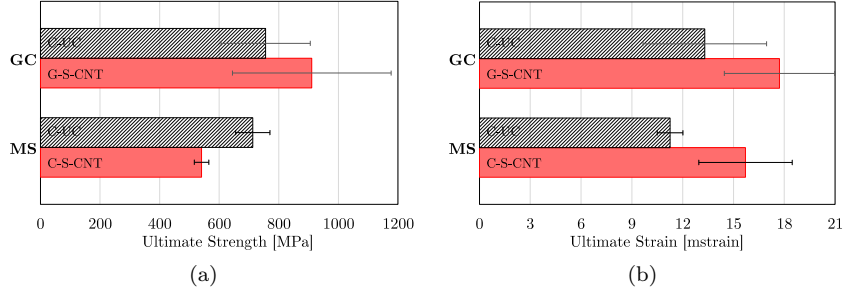

Figure 11: Mean ultimate strength (a) and strain (b) with ± 1 standard deviation bands for uncoated (UC, grey) and coated (S-CNT, red) carbon fabric reinforced specimens

For better comparison, bar-charts are given in Figure 11 which illustrate ultimate performance alongside standard deviation bands for the MS and GC mortars. Data on mean ultimate strength, elongation and specific energy dissipated at failure are gathered in Table 5, where the percentage variance is also given. Again, characteristic values are computed following Eqn.(1).

In general, a positive effect is still brought by CNT-coating on carbon fabric specimens. However, data scattering shows a mixed response. Interestingly, S-CNT coating is most advantageous for mortar G, which is characterized by higher nominal compressive strength and stiffness and lower nominal ductility. This seems to partly contrast the observations drawn by Signorini et al. [46], according to which best performance is associated to higher lime content in the binder. However, in contrast to the present study, Signorini et al. [46] employ a high compressive strength mortar which contains glass microfibers. Indeed, the benefit of adding dispersed microfibres to the mortar in terms of tensile response is well-documented in the literature [57, 58]. It is therefore concluded that mechanical performance in traction of the embedding mortar plays a fundamental role in determining the overall tensile response of the composite.

In the case of both mortars, coating brings about a significant increase in the mean ultimate elongation, that is +40% for MS and +33% for GC. In terms of ultimate strength, coating induces an unexpected 24% UTS loss for mortar MS.

17

	UC				S-CNT				Δ	
m	$\mu(f_u)$ [MPa]	$\varsigma(f_u)$ [MPa]	CoV [%]	$f_{u,k}$ [MPa]	$\mu(f_u)$ [MPa]	$\varsigma(f_u)$ [MPa]	CoV [%]	$f_{u,k}$ [MPa]	Δf_m [%]	$\Delta f_{u,k}$ [%]
MS	713	58	8	618	540	24	5	501	-24	-19
GC	756	150	20	510	911	266	29	475	+20	-7
	$\mu(\varepsilon_u)$ [mstrain]	$\varsigma(\varepsilon_u)$ [mstrain]	CoV [%]	$\varepsilon_{u,k}$ [mstrain]	$\mu(\varepsilon_u)$ [mstrain]	$\varsigma(\varepsilon_u)$ [mstrain]	CoV [%]	$\varepsilon_{u,k}$ [mstrain]	$\Delta\varepsilon_m$ [%]	$\Delta\varepsilon_{u,k}$ [%]
MS	11.3	0.8	7	10	15.7	2.8	18	11.1	+40	+11
GC	13.3	3.7	27	7.2	17.7	3.3	18	12.3	+33	+70
	$\mu(W_u)$ [J/mm^3]	$\varsigma(W_u)$ [J/mm^3]	CoV [%]	$W_{u,k}$ [J/mm^3]	$\mu(W_u)$ [J/mm^3]	$\varsigma(W_u)$ [J/mm^3]	CoV [%]	$W_{u,k}$ [J/mm^3]	ΔW_m [%]	$\Delta W_{u,k}$ [%]
MS	3.94	0.40	10	3.28	4.91	1.05	21	3.19	+25	-3
GC	8.74	3.06	35	3.72	23.54	11.64	49	4.45	+169	+20

Table 5: Carbon reinforcement – Mean ultimate tensile strength $\mu(f_u)$, mean strain $\mu(\varepsilon_u)$ and mean dissipated energy $\mu(W_u)$ across all tested groups, alongside their standard deviation ς, coefficient of variation CoV and percent variance Δ. $f_{u,k}$ is the characteristic strength in a normal distribution

However, this detrimental bearing is outweighed by ductility enhancement so that the combined effect works out beneficial on toughness (i.e. energy dissipation), that is still improved of about 25%. The outcome is far more impressive for GC mortar, for which toughness increases by 169%, ductility by 70% and UTS by a mere +20%.
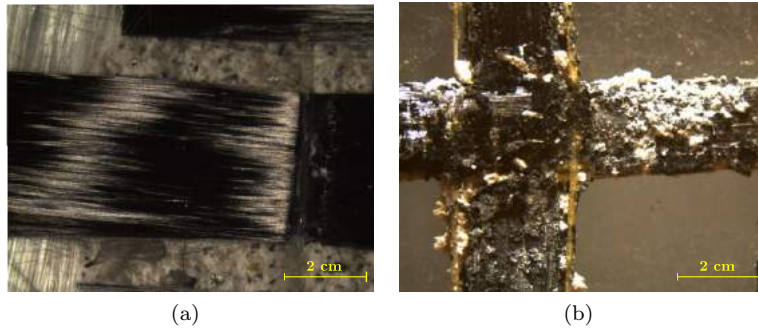

Figure 12: 8X magnification of uncoated (a) and coated (b) carbon yarns at failure.

Optical microscopy depicts a scenario that is consistent with the findings provided by mechanical tests. Fig.12 and 13 show fibres emerging from failed C-TRM specimens with GC mortar at 8X and 35X magnification, respectively.
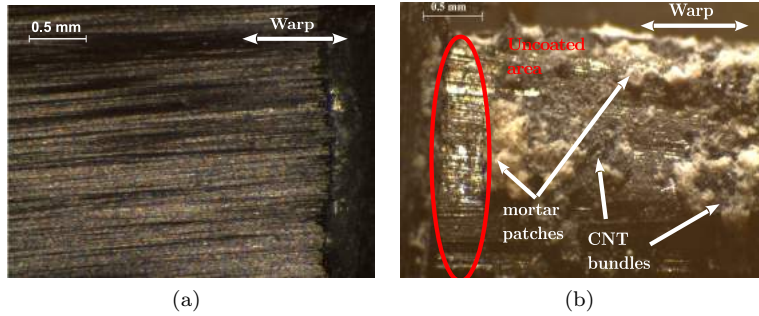
Figure 13: 35X magnification of uncoated (a) and coated (b) carbon yarns at failure.
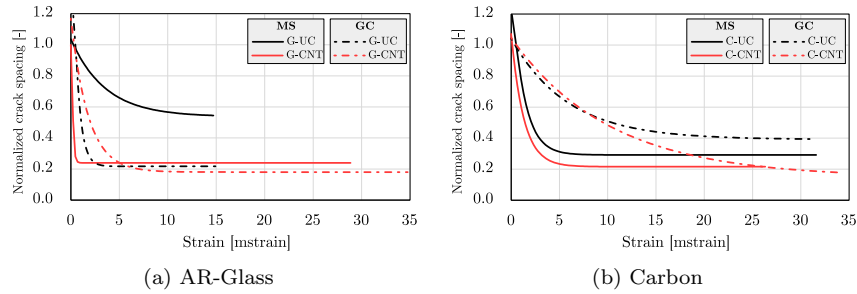

Figure 14: Mean crack spacing (data fit) as a function of strain during testing of AR-glass (a) and carbon (b) specimens in GC mortar. Uncoated specimens are represented with black lines, whilst S-CNT ones with red lines. For the sake of comparison, relevant groups have the same line type (e.g. solid for GC mortar and dash-dotted for MS mortar).

Despite generally good impregnation of the coated yarns, supported by the presence of diffuse mortar patches on the surface, wide zones still exist where the coating is not attached any mortar grain (see detail in Figure 13(b)). These areas suggest random lack of adhesion, possibly accompanied by the occurrence of slippage, and either phenomenon is attached to large data scattering. Also, the strength curve exhibits a blurred behaviour where the three stages are no longer well distinct.

3.3. Crack analysis

The evolution of the crack pattern during tensile testing provides information about incipient damage mechanisms correlated with matrix-to-fabric adhesion. Two important features are identified by DIC post-processing: the average crack spacing, which is related with the interphase bond and the apparent composite

19

Mortar/Fabric	UC			S-CNT		
	S_1 [mm]	α [-]	R^2 [-]	S_1 [mm]	α [-]	R^2 [-]
MS/G	123.5	0.28	0.985	55.0	8.09	1.000
MS/C	67.2	0.79	0.976	49.7	0.77	0.953
GC/G	50.0	1.78	1.000	41.5	0.56	0.991
GC/C	90.0	0.17	0.979	33.6	0.10	0.964

Table 6: Parameters for the mean crack spacing Eq.(2), as obtained by data fitting

stiffness [59], and the average crack width. The latter strongly affects durability, for serviceability of structures is endangered by extensive crack opening. Fig.14 illustrates the evolution of the crack spacing, that is the mean spacing between two adjacent cracks. Data are fitted, as a function of strain, to an exponential model proposed by Mobasher [2] and successively adopted by Signorini et al. [52] for durability considerations

$$S(\varepsilon) = S_1 + S_0 \exp\left[-\alpha(\varepsilon - \varepsilon_1)\right], \qquad \varepsilon \geq \varepsilon_1. \tag{2}$$

Here, S_1 represents the saturation value for crack spacing, that is an important index of interphase strength, ε_1 is the first strain value in the dataset and $S(\varepsilon_1) = S_0 + S_1$ the corresponding spacing. The decay parameter α and the characteristic saturation mean crack spacing S_1 are fitted for each group and reported in Table 6. Better performance is associated to lower saturation crack distances, implying a diffused crack pattern. Indeed, as already discussed, all coated groups consistently present several closely-spaced cracks, as opposed to uncoated specimens for which a few far-spaced cracks appear. Interpretation of the decaying exponent α, which indicates the capacity of the laminate to crack at an early stage, appears more difficult. Indeed, α appears little changing, with the noticeable exception of a striking increase occurring for G fabric in MS mortar. For carbon-based systems, the index is not significantly modified by the coating, while, for GC/G, a slight reduction is found. Such fluctuations can be ascribed to the coexistence of several competing cracking mechanisms, also in the brittle matrix, and to the confining effect of the gripping system in the test
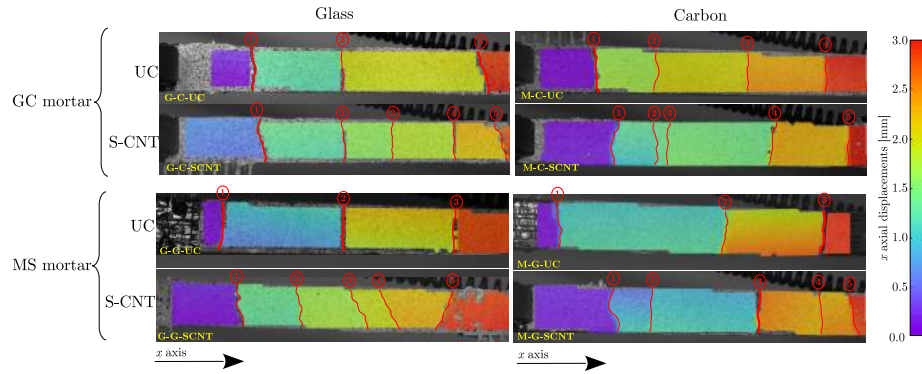
Figure 15: Longitudinal displacement colour map, obtained by DIC post processing, at fixed elongation $\bar{\varepsilon} = 13$ mstrain, for uncoated (upper) and S-CNT coated (lower) TRM specimens
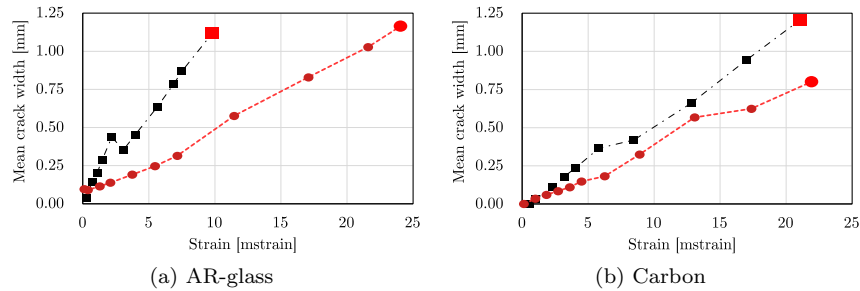

(a) AR-glass

(b) Carbon

Figure 16: Mean crack width as a function of strain during testing for AR-glass (a) and carbon (b) samples for MS mortar. Uncoated samples are represented by grey dash-dotted lines and square markers, whilst S-CNT specimen behaviour is denoted by circular markers connected by violet dotted lines

set-up [60]. Fig.15 presents a colour map description of the displacement field in the longitudinal direction and compares coated with uncoated samples at the prescribed strain level $\bar{\varepsilon} = 13$ mstrain. The presence of cracks is highlighted in red colour. While uncoated specimens present a coarse crack pattern, with few large cracks spanning the direction y orthogonal to the loading, coated coupons exhibit a diffused pattern of fine cracks throughout the gauge length. This behaviour is directly associated to enhanced adhesion, consistently to the findings presented in previous papers and related to plain nano-silica coating [51] and to epoxy coating [17].

The same pattern is described by Figures 16 and 17, where the evolution of the average crack width and of the average crack spacing is presented as a
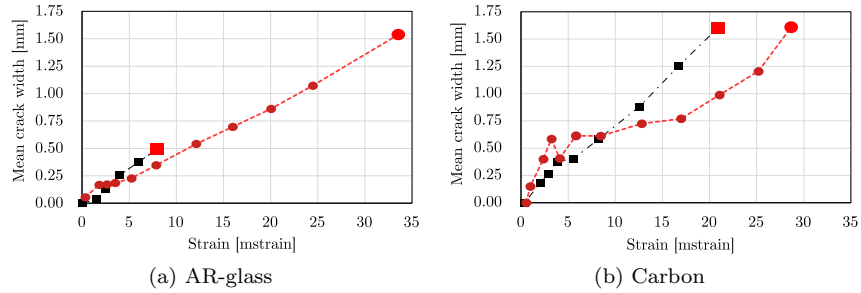
21

(a) AR-glass (b) Carbon

Figure 17: Mean crack width as a function of strain during testing for AR-glass (a) and carbon (b) samples for GC mortar. Uncoated samples are represented with grey dash-dotted lines and square markers, whilst S-CNT ones with violet dotted lines and circular markers.

function of strain. Comparing coated and uncoated specimens for any fixed value of strain (namely, at the same instant of the test) after the cracking stage, the former present lower values than the latter for both indices.

4. Conclusions

(a) (b)
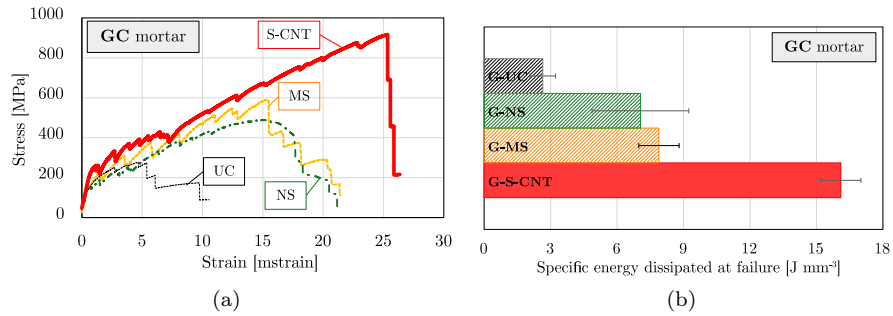
Figure 18: Comparison, in terms of mean strength curves (a) and mean specific energy dissipated at failure (b), for different coating strategies applied to AR-glass in mortar GC: no coating (UC), nanosilica (NS), microsilica (MS) and silica+MWCNTs (S-CNT). Results for microsilica and nanosilica are taken from [21] and [46], respectively

We analyse the application of a mineral silica sol-gel coating, loaded with dispersed multi-walled carbon nanotubes (MWCNTs), to AR-glass and carbon Textile Reinforced Mortar composites for structural purposes. Two inorganic lime-based mortars at 56-day curing are considered as embedding medium. Remarkable gains in terms of mechanical performance are highlighted in uni-axial traction tests, especially with respect to glass fabric. Investigation of the chem-

22

ical adhesion at the fibres-to-matrix interphase, through optical and E-SEM microscopy, supports the role of the coating in preventing delamination and telescopic failure. The following conclusions can be drawn:

- Silica coating takes advantage of pozzolanic reactivity in the neighbourhood of the thin mortar layer surrounding the fabric yarns (i.e. the so-called interphase transition zone) [61];

- The addition of well-dispersed MWCNTs produces a two-fold increase, in terms of strength, with respect to the already significant contribution of plain-vanilla silica coating; thus, an almost optimal performance is attained, that scores slightly below the tensile strength of the dry glass fabric (i.e. around 1200 MPa);

- For AR-glass embedded in GC mortar, Fig.18 compares, in terms of strength curves (a) and specific dissipated energy at failure (b), the present findings with the outcome of different coating strategies, pertaining to micro-silica [46] and nano-silica [21] sol-gel. It shows that adding CNTs roughly double the best outcome both in terms of strength and energy dissipation;

- CNTs provide a striking increase in the specific surface area (SSA) of the reinforcement and effectively roughen its surface. The resulting composite system exhibits a diffuse crack pattern, with high dissipation capability, and a prolonged cracking stage associated to several small stress drops in the strength curve.

- Coating successfully prevents delamination and telescopic failure, whence it warrants consistent performance (narrows data scattering), to great advantage of design limits;

- Sol-gel coating is especially effective for AR-glass, while mixed results are retrieved for carbon;

- Matrix composition strongly affects the overall behaviour, with stronger binders being, in general, better performing;

- The inorganic nature of the coating (as opposed to epoxy coating) preserves the attractive features connected to TRM materials.

Acknowledgements

Funding

Declaration of interest

None

References

[1] Carloni, C., Bournas, D.A., Carozzi, F.G., D'Antino, T., Fava, G., Focacci, F., et al. Fiber reinforced composites with cementitious (inorganic) matrix. In: Design procedures for the use of composites in strengthening of reinforced concrete structures. Springer; 2016, p. 349–392.

[2] Mobasher, B.. Mechanics of fiber and textile reinforced cement composites. CRC press; 2011.

[3] D'Antino, T., Carloni, C., Sneed, L., Pellegrino, C.. Matrix–fiber bond behavior in PBO FRCM composites: A fracture mechanics approach. Engineering Fracture Mechanics 2014;117:94–111.

[4] D'Antino, T., Pellegrino, C., Carloni, C., Sneed, L.H., Giacomin, G.. Experimental analysis of the bond behavior of glass, carbon, and steel FRCM composites. In: Key engineering materials; vol. 624. Trans Tech Publ; 2015, p. 371–378.

[5] Nobili, A., Falope, F.O.. Impregnated carbon fabric–reinforced cementitious matrix composite for rehabilitation of the finale emilia hospital roofs: Case study. Journal of composites for construction 2017;21(4):05017001.

[6] Bunsell, A.R., Renard, J.. Fundamentals of fibre reinforced composite materials. CRC Press; 2005.

[7] Carozzi, F., Poggi, C.. Mechanical properties and debonding strength of fabric reinforced cementitious matrix (frcm) systems for masonry strengthening. Composites Part B: Engineering 2015;70:215–230.

[8] Carozzi, F.G., Colombi, P., Fava, G., Poggi, C.. A cohesive interface crack model for the matrix–textile debonding in frcm composites. Composite Structures 2016;143:230–241.

[9] Täljsten, B., Blanksvärd, T.. Mineral-based bonding of carbon FRP to strengthen concrete structures. Journal of Composites for Construction 2007;11(2):120–128.

[10] Donnini, J., Corinaldesi, V., Nanni, A.. Mechanical properties of FRCM using carbon fabrics with different coating treatments. Composites Part B: Engineering 2016;88:220–228.

[11] Siddique, R., Mehta, A.. Effect of carbon nanotubes on properties of cement mortars. Construction and Building Materials 2014;50:116–129.

[12] Irshidat, M.R., Al-Shannaq, A.. Using textile reinforced mortar modified with carbon nano tubes to improve flexural performance of RC beams. Composite Structures 2018;200:127–134.

25

[13] ACI 549.4R-13, . Guide to Design and Construction of Externally Bonded Fabric-Reinforced Cementitious Matrix (FRCM) Systems for Repair and Strengthening Concrete and Masonry Structures. American Concrete Institute; 2013.

[14] Mercedes, L., Gil, L., Bernat-Maso, E.. Mechanical performance of vegetal fabric reinforced cementitious matrix (FRCM) composites. Construction and Building Materials 2018;175:161–173.

[15] Dvorkin, D., Poursaee, A., Peled, A., Weiss, W.. Influence of bundle coating on the tensile behavior, bonding, cracking and fluid transport of fabric cement-based composites. Cement and Concrete Composites 2013;42:9–19.

[16] Scheffler, C., Gao, S., Plonka, R., Mäder, E., Hempel, S., Butler, M., et al. Interphase modification of alkali-resistant glass fibres and carbon fibres for textile reinforced concrete I: Fibre properties and durability. Composites Science and Technology 2009;69(3):531–538.

[17] Messori, M., Nobili, A., Signorini, C., Sola, A.. Mechanical performance of epoxy coated AR-Glass fabric Textile Reinforced Mortar: Influence of coating thickness and formulation. Composites Part B: Engineering 2018;149:135–143.

[18] Signorini, C., Nobili, A., Sola, A., Messori, M.. Designing epoxy viscosity for optimal mechanical performance of coated glass textile reinforced mortar (gtrm) composites. Construction and Building Materials 2020;233:117325.

[19] Messori, M., Nobili, A., Signorini, C., Sola, A.. Effect of high temperature exposure on epoxy-coated Glass Textile Reinforced Mortar (GTRM) composites. Construction and Building Materials 2019;212:765–774.

[20] Amraei, J., Jam, J.E., Arab, B., Firouz-Abadi, R.D.. Effect of interphase zone on the overall elastic properties of nanoparticle-reinforced polymer nanocomposites. Journal of Composite Materials 2019;53(9):1261–1274.

26

[21] Signorini, C., Sola, A., Nobili, A., Siligardi, C.. Lime-cement textile reinforced mortar (TRM) with modified interphase. The Journal of Applied Biomaterials and Functional Materials 2019;17(1). doi:10.1177/2280800019827823.

[22] Nadiv, R., Peled, A., Mechtcherine, V., Hempel, S., Schroefl, C.. Micro-and nanoparticle mineral coating for enhanced properties of carbon multifilament yarn cement-based composites. Composites Part B: Engineering 2017;111:179–189.

[23] Cohen, Z., Peled, A.. Effect of nanofillers and production methods to control the interfacial characteristics of glass bundles in textile fabric cement-based composites. Composites Part A: Applied Science and Manufacturing 2012;43(6):962–972.

[24] Hakamy, A., Shaikh, F., Low, I.M.. Microstructures and mechanical properties of hemp fabric reinforced organoclay–cement nanocomposites. Construction and Building Materials 2013;49:298–307.

[25] Franchini, M., Fabbri, P., Frache, A., Ori, G., Messori, M., Siligardi, C., et al. Bentonite-based organoclays as innovative flame retardants agents for SBS copolymer. Journal of nanoscience and nanotechnology 2008;8(12):6316–6324.

[26] Hapuarachchi, T.D., Peijs, T.. Multiwalled carbon nanotubes and sepiolite nanoclays as flame retardants for polylactide and its natural fibre reinforced composites. Composites Part A: Applied Science and Manufacturing 2010;41(8):954–963.

[27] Oberlin, A., Endo, M., Koyama, T.. Filamentous growth of carbon through benzene decomposition. Journal of crystal growth 1976;32(3):335–349.

[28] Iijima, S.. Helical microtubules of graphitic carbon. Nature 1991;354(6348):56.

27

[29] Schadler, L., Giannaris, S.,, , Ajayan, P.. Load transfer in carbon nanotube epoxy composites. Applied physics letters 1998;73(26):3842–3844.

[30] Treacy, M.J., Ebbesen, T., Gibson, J.. Exceptionally high young's modulus observed for individual carbon nanotubes. nature 1996;381(6584):678–680.

[31] Kostopoulos, V., Baltopoulos, A., Karapappas, P., Vavouliotis, A., Paipetis, A.. Impact and after-impact properties of carbon fibre reinforced composites enhanced with multi-wall carbon nanotubes. Composites Science and Technology 2010;70(4):553–563.

[32] Liew, K., Kai, M., Zhang, L.. Carbon nanotube reinforced cementitious composites: An overview. Composites Part A: Applied Science and Manufacturing 2016;91:301–323.

[33] Liew, K., Kai, M., Zhang, L.. Mechanical and damping properties of CNT-reinforced cementitious composites. Composite Structures 2017;160:81–88.

[34] Nochaiya, T., Chaipanich, A.. Behavior of multi-walled carbon nanotubes on the porosity and microstructure of cement-based materials. Applied Surface Science 2011;257(6):1941–1945.

[35] Stynoski, P., Mondal, P., Marsh, C.. Effects of silica additives on fracture properties of carbon nanotube and carbon fiber reinforced portland cement mortar. Cement and Concrete Composites 2015;55:232–240.

[36] Cui, X., Han, B., Zheng, Q., Yu, X., Dong, S., Zhang, L., et al. Mechanical properties and reinforcing mechanisms of cementitious composites with different types of multiwalled carbon nanotubes. Composites Part A: Applied Science and Manufacturing 2017;103:131–147.

[37] Han, B., Zhang, L., Zeng, S., Dong, S., Yu, X., Yang, R., et al. Nano-core effect in nano-engineered cementitious composites. Composites Part A: Applied Science and Manufacturing 2017;95:100–109.

28

[38] Konsta-Gdoutos, M.S., Aza, C.A.. Self sensing carbon nanotube (CNT) and nanofiber (CNF) cementitious composites for real time damage assessment in smart structures. Cement and Concrete Composites 2014;53:162–169.

[39] Loh, K.J., Gonzalez, J.. Cementitious composites engineered with embedded carbon nanotube thin films for enhanced sensing performance. In: Journal of Physics: Conference Series; vol. 628. IOP Publishing; 2015, p. 012042.

[40] Irshidat, M.R., Al-Shannaq, A.. Bond strength evaluation between textiles reinforced mortar with carbon nanotubes and concrete substrate. Latin American Journal of Solids and Structures 2019;16(9).

[41] Peigney, A., Laurent, C., Flahaut, E., Bacsa, R., Rousset, A.. Specific surface area of carbon nanotubes and bundles of carbon nanotubes. Carbon 2001;39(4):507–514.

[42] Yazdanbakhsh, A., Grasley, Z., Tyson, B., Al-Rub, R.K.A.. Distribution of carbon nanofibers and nanotubes in cementitious composites. Transportation Research Record 2010;2142(1):89–95.

[43] Parveen, S., Rana, S., Fangueiro, R., Paiva, M.C.. Microstructure and mechanical properties of carbon nanotube reinforced cementitious composites developed using a novel dispersion technique. Cement and Concrete Research 2015;73:215–227.

[44] Haghgoo, M., Yousefi, A.A., Mehr, M.J.Z., Celzard, A., Fierro, V., Léonard, A., et al. Characterization of multi-walled carbon nanotube dispersion in resorcinol–formaldehyde aerogels. Microporous and Mesoporous Materials 2014;184:97–104.

[45] Rastogi, R., Kaushal, R., Tripathi, S., Sharma, A.L., Kaur, I., Bharadwaj, L.M.. Comparative study of carbon nanotube dispersion using surfactants. Journal of colloid and interface science 2008;328(2):421–428.

[46] Signorini, C., Nobili, A., Siligardi, C.. Sustainable mineral coating of alkali-resistant glass fibres in textile-reinforced mortar composites for structural purposes. Journal of Composite Materials 2019;53(28–30):4203–4213.

[47] Brunauer, S., Emmett, P.H., Teller, E.. Adsorption of gases in multi-molecular layers. Journal of the American chemical society 1938;60(2):309–319.

[48] ICC AC434, . Acceptance criteria for masonry and concrete strengthening using fiber-reinforced cementitious matrix (FRCM) composite systems. Tech. Rep.; International Code Council; 2013.

[49] Consiglio Superiore dei Lavori Pubblici, . Linea guida per la identificazione, la qualificazione ed il controllo di accettazione di compositi fibrorinforzati a matrice inorganica (FRCM) da utilizzarsi per il consolidamento strutturale di costruzioni esistenti. Italian Standard for the Qualification of FRCM composite systems for externally bonded reinforcement of existing structures; Consiglio Superiore dei Lavori Pubblici; 2019.

[50] Nobili, A., Signorini, C.. On the effect of curing time and environmental exposure on impregnated Carbon Fabric Reinforced Cementitious matrix (CFRCM) composite with design considerations. Composites Part B: Engineering 2017;112:300–313.

[51] Signorini, C., Nobili, A., Cedillo Gonzalez, E.I., Siligardi, C.. Silica coating for interphase bond enhancement of carbon and AR-Glass Textile Reinforced Mortar (TRM). Composites Part B: Engineering 2018;141:191–202.

[52] Signorini, C., Nobili, A., Falope, F.O.. Mechanical performance and crack pattern analysis of aged Carbon Fabric Cementitious Matrix (CFRCM) composites. Composite Structures 2018;202:1114 – 1120. Special issue dedicated to Ian Marshall.

[53] RILEM 232-TDT, . Test methods and design of textile reinforced concrete. Tech. Rep. 12; International Union of Laboratories and Experts in Construction Materials, Systems and Structures; 2016. doi:10.1617/s11527-016-0839-z.

[54] Nobili, A.. Durability assessment of impregnated glass fabric reinforced cementitious matrix (GFRCM) composites in the alkaline and saline environments. Construction and Building Materials 2016;105:465–471.

[55] Mobasher, B., Peled, A., Pahilajani, J.. Distributed cracking and stiffness degradation in fabric-cement composites. Materials and structures 2006;39(3):317–331.

[56] Mandel, J.. The statistical analysis of experimental data. Dover Publishing Inc; 2012.

[57] De Santis, S., de Felice, G.. Steel reinforced grout systems for the strengthening of masonry structures. Composite Structures 2015;134:533–548.

[58] Shu, X., Graham, R.K., Huang, B., Burdette, E.G.. Hybrid effects of carbon fibers on mechanical properties of portland cement mortar. Materials & Design (1980-2015) 2015;65:1222–1228.

[59] Falope, F., Lanzoni, L., Tarantino, A.. Modified hinged beam test on Steel Fabric Reinforced Cementitious Matrix (SFRCM). Composites Part B: Engineering 2018;146:232–243.

[60] Arboleda, D., Babaeidarabad, S., Hays, C., Nanni, A.. Durability of fabric reinforced cementitious matrix (FRCM) composites. In: Proceedings of the 7th International Conference on FRP Composites in Civil Engineering. International Institute for FRP in Construction (IIFC); 2014,Vancouver, 20-22 August 2014.

[61] Jo, B.W., Kim, C.H., Tae, G.h., Park, J.B.. Characteristics of cement mortar with nano-SiO2 particles. Construction and building materials 2007;21(6):1351–1355.